Vibrational renormalisation of the electronic band gap in hexagonal and cubic ice

Edgar A. Engel,[1,*] Bartomeu Monserrat,[1,2] and Richard J. Needs[1]

[1] *TCM Group, Cavendish Laboratory, University of Cambridge, J. J. Thomson Avenue, Cambridge CB3 0HE, United Kingdom*

[2] *Department of Physics and Astronomy, Rutgers University, Piscataway, New Jersey 08854-8019, USA*

(Dated: October 8, 2018)

Electron-phonon coupling in hexagonal and cubic water ice is studied using first-principles quantum mechanical methods. We consider 29 distinct hexagonal and cubic ice proton-orderings with up to 192 molecules in the simulation cell to account for proton-disorder. We find quantum zero-point vibrational corrections to the minimum electronic band gaps ranging from −1.5 to −1.7 eV, which leads to improved agreement between calculated and experimental band gaps. Anharmonic nuclear vibrations play a negligible role in determining the gaps. Deuterated ice has a smaller band-gap correction at zero-temperature of −1.2 to −1.4 eV. Vibrations reduce the differences between the electronic band gaps of different proton-orderings from around 0.17 eV to less than 0.05 eV, so that the electronic band gaps of hexagonal and cubic ice are almost independent of the proton-ordering when quantum nuclear vibrations are taken into account. The comparatively small reduction in the band gap over the temperature range 0–240 K of around 0.1 eV does not depend on the proton ordering, or whether the ice is protiated or deuterated, or hexagonal or cubic. We explain this in terms of the atomistic origin of the strong electron-phonon coupling in ice.

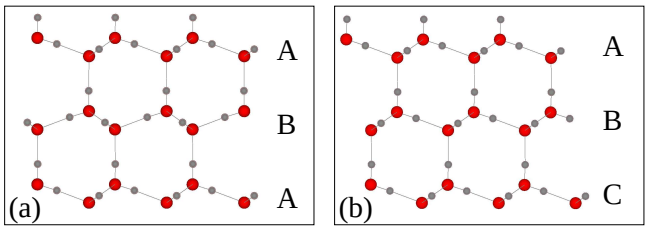

FIG. 1. The oxygen sublattices of (a) hexagonal, Ih, and (b) cubic ice, Ic, are shown in red. The puckered layers have ABAB and ABC stackings in Ih and Ic, respectively. Arbitrarily chosen particular proton-orderings obeying the Bernal-Fowler ice rules are shown in grey.

I. INTRODUCTION

Ice is a key constituent of the Earth's crust and mantle [1, 2], while on its surface and in its atmosphere it plays a crucial role in the water cycle and in determining climate [3–5]. Accordingly, ice is one of the experimentally and computationally most extensively studied condensed matter systems and its properties have been investigated across a wide range of temperatures and pressures [3].

The electronic bandstructure of ice plays an important role, e.g., in the redox reactions of atmospheric chemistry [6–15], in glaciers [16], Earth's interior [2, 17, 18], and in structural determinations using electrochemical scanning tunnelling microscopy in aqueous environments [19]. The insulator to metal transition induced by band gap closure [20–25] in high pressure ice phases is thought to be important in astrophysical contexts such as in the sources of the magnetic fields of Uranus and Neptune [26].

* eae32@cam.ac.uk

At the pressures found on Earth's surface only stable hexagonal (Ih) and meta-stable cubic ice (Ic) [27] (see Fig. 1) occur naturally. The latter typically contains many stacking faults. While experimental estimates of the zero-temperature electronic quasi-particle band gap, $E_g(0)$, in Ih of 8.8 ± 0.4 eV exist (see Refs. [29–35] and references therein), reliable values for Ic do not, since high purity samples of Ic have not been synthesised.

First-principles electronic structure calculations can be used to study electronic band structures, and quasi-particle and excitonic band gaps. However, density functional theory (DFT) using semi-local functionals – the workhorse of modern day electronic structure calculations – normally underestimates band gaps. Much progress has been made in calculating electronic band gaps using more accurate but computationally demanding hybrid functionals [36], screened exchange functionals [37], perturbation theories such as the *GW* approximation [38–42], and quantum chemical [43, 44] and quantum Monte Carlo techniques [45–49]. *GW* calculations for proton-ordered hexagonal ice (XIh), for example, reproduce the experimentally observed optical absorption spectra of Ih reasonably well in comparison to semi-local DFT [29, 30]. However, *GW* results for hexagonal ice of 9.6 ± 0.4 eV [29, 30] overestimate E_g by around 1 eV.

Nuclear vibrations and proton-ordering are often neglected in studying band gaps of water and ice, but these effects have remarkable consequences for the electronic bandstructure ([25, 50] and this work). Measurements of band gaps of water provide strong experimental evidence for the importance of nuclear vibrations [51]. In liquid water, E_g depends strongly on temperature which indicates large thermal vibrational effects and suggests large zero-point (ZP) quantum vibrational effects [25, 51, 52]. This observation motivates us to investigate whether vibrational effects could play a significant role in explaining the discrepancy between the values of E_g obtained within

the *GW* approximation and experiment. We have previously reported strong electron-phonon coupling in various molecular crystals, amongst them a proton-ordering of Ih with $P6_3cm$ symmetry [50]. Benchmarking computational models against experimentally accessible systems, such as ice under ambient pressure, is essential. Ice displays a range of important and interesting phenomena related to configurational disorder and strong effects from nuclear vibrations due to the light hydrogen nuclei, which must both be included to obtain accurate atomistic simulations.

In this work we focus on vibrational corrections to the electronic band gaps of Ih and Ic, accounting for quantum nuclear vibrations and thermal effects (Sec. III). We investigate the effects of replacing the hydrogen atoms in Ih and Ic by heavier deuterons (Sec. IV), evaluate the role of vibrational anharmonicity (Sec. V), and determine the atomistic origins of the strong electron-phonon coupling (Sec. VI).

II. COMPUTATIONAL MODEL

A. Stacking faults and proton-disorder

It was long believed that ice at ambient pressure occurs in the hexagonal (Ih) and cubic (Ic) forms shown in Fig. 1. Both Ih and Ic consist of tetrahedrally coordinated water molecules satisfying the "Bernal-Fowler ice rules" [53]. Ih and Ic have very similar free energies [27] and their structures differ only in the stacking of the atomic layers (see Fig. 1). Thermodynamically stable Ih occurs naturally in abundance and plays a key role in determining Earth's climate [3–5]. The metastable, ideal Ic form [54] was also thought to play a role in nature, but to be very rare [55, 56]. However, real "cubic ice" typically contains many stacking faults and is therefore now referred to as stacking-disordered ice (Isd). Isd refers to the infinite set of possible stacking sequences, which smoothly connects Ih as one end member to Ic as the other. Isd is a highly complex material [57–59] and is thought to play a key role in ice nucleation, a process central to climate. A full understanding of Isd will require knowledge of the properties of Ih and Ic, which we limit ourselves to in this study.

Ih and Ic are proton-disordered systems with an extensive ground-state degeneracy that leads to Pauling's residual configurational entropy [60–62]. Atomistic simulations of Ih and Ic treat the hydrogen atoms explicitly and are based on representative sets of energetically quasi-degenerate, proton-ordered structures. The number of such structures allowed by the ice rules increases exponentially with the size of the simulation cell. For large systems, the configurational entropies of Ih and Ic are found to be almost identical [63, 64], and therefore they do not affect the relative stability.

We consider 16 distinct proton-ordered eight-molecule Ih configurations as constructed by Hirsch and Ojamäe [65], and 11 distinct proton-ordered eight-molecule Ic configurations [66]. We also consider the "conventional" hexagonal, 12-molecule $P6_3cm$ Ih and quasi-cubic, eight-molecule $P4_3$ Ic structures (numbers 13 and 1 in Figs. 5 (a) and (b), respectively). We calculate differences in static lattice energies for these sets of Ih and Ic proton-orderings which are in good agreement with those in Refs. [65, 67]. More importantly, the variations in static lattice energies across the Ih proton-orderings agree with those calculated using first principles methods in Ref. [68] for a much larger set of 16 8-molecule orthorhombic, 14 12-molecule hexagonal and 63 48-molecule orthorhombic Ih proton-orderings. These results strongly suggest that our sets of proton-orderings provide a good representation of proton-disordered Ih and Ic.

B. Static lattice calculations

While DFT with semi-local exchange-correlation functionals underestimates static electronic band gaps, it performs well in evaluating phonon spectra and vibrational band-gap corrections in ice, see Supplementary Section V [69] for details. We performed electronic structure calculations using plane-wave pseudopotential DFT as implemented in the CASTEP code [70] (version 7.02). We employed the Perdew-Burke-Ernzerhof (PBE) [71, 72] semilocal generalised gradient approximation functional, and on-the-fly generated ultrasoft pseudopotentials [73] with core radii of 0.7 Å and 0.8 Å for the hydrogen and oxygen atoms, respectively. We used a plane-wave energy cut-off of 1600 eV and Monkhorst-Pack electronic reciprocal space grids of spacing less than $2\pi \times 0.04$ Å^{-1} for the total energy calculations and geometry optimisations involved in the vibrational calculations described in Section II C. The resulting energy differences between frozen-phonon configurations are converged to within 10^{-4} eV/H_2O, the atomic positions are converged to within 10^{-5}Å, and the residual forces to within 10^{-4} eV/Å. We used a lower plane-wave energy cut-off of 800 eV for the band structure calculations of frozen-phonon structures, which is sufficient for accurate electron-phonon coupling calculations as described in Section II D.

C. Vibrational calculations

We obtained the harmonic vibrational normal modes, which define the normal phonon coordinates $q_{n\mathbf{k}}$ and the harmonic vibrational frequencies $\omega_{n\mathbf{k}}$ of a vibrational mode $(n, \mathbf{k})$, using a finite displacement method [74]. n and $\mathbf{k}$ denote the branch index and vibrational Brillouin Zone wavevector of the vibrational mode, respectively. The phonon coordinates $q_{n\mathbf{k}}$ denote the atomic displacements along the vibrational mode $(n, \mathbf{k})$. Anharmonic vibrations were calculated using the method described in Ref. [75]. We investigate the $3N$-dimensional BO en-

ergy surface (where N is the number of atoms in the simulation cell) by mapping 1D subspaces along the harmonic normal mode axes. Using 11 equally spaced sampling points for each 1D subspaces was found to lead to converged results. Large maximum amplitudes of four times the harmonic root-mean-square (RMS) displacements were chosen to accurately describe the BO energy surface where anharmonicity is important. We then construct the $3N$-dimensional BO surface from the 1D subspaces which were fitted using cubic splines [27]. The anharmonic vibrational Schrödinger equation was solved within a vibrational self-consistent field (VSCF) framework. The anharmonic vibrational wave function was expanded as a Hartree product,

$$|\phi_{\mathbf{S}}(\mathbf{q})\rangle = \prod_{n,\mathbf{k}} |\varphi_{S_{n\mathbf{k}}}(q_{n\mathbf{k}})\rangle \ , \tag{1}$$

of single-particle anharmonic eigenstates, $|\varphi_{S_{n\mathbf{k}}}(q_{n\mathbf{k}})\rangle$, with energy $\mathrm{E}_{S_{n\mathbf{k}}}$. $\mathbf{S}$ denotes the vibrational eigenstate whose elements $S_{n\mathbf{k}}$ label the states of the vibrational modes $(n, \mathbf{k})$. In practice, we expand the anharmonic states $|\varphi_{S_{n\mathbf{k}}}(q_{n\mathbf{k}})\rangle$ in a basis of simple harmonic oscillator eigenstates. The inclusion of 25 simple harmonic oscillator states for each degree of freedom was found to lead to converged results (see Supplementary Section I).

D. Electron-phonon coupling

Within the Born-Oppenheimer approximation, the vibrationally corrected band gap, $E_g(T)$, at temperature T may be written as

$$E_g(T) = \frac{1}{Z(T)} \sum_{\mathbf{S}} \langle\phi_{\mathbf{S}}(\mathbf{q})| \hat{E}_g(\mathbf{q}) |\phi_{\mathbf{S}}(\mathbf{q})\rangle \exp\left(-\beta \mathrm{E}_{\mathbf{S}}\right), \tag{2}$$

where

$$Z(T) = \sum_{\mathbf{S}} \langle\phi_{\mathbf{S}}(\mathbf{q})|\phi_{\mathbf{S}}(\mathbf{q})\rangle \exp\left(-\beta \mathrm{E}_{\mathbf{S}}\right), \ \beta = 1/k_{\mathrm{B}}T \tag{3}$$

is the partition function, $\hat{E}_g(\mathbf{q})$ is the gap for a frozen phonon structure with atomic positions $\mathbf{q} = (\ldots, q_{n\mathbf{k}}, \ldots)$, and $|\phi_{\mathbf{S}}(\mathbf{q})\rangle$ is the harmonic or (where explicitly stated) anharmonic vibrational eigenstate with energy $\mathrm{E}_{\mathbf{S}}$. The summation over vibrational eigenstates $\mathbf{S}$ includes the vibrational ground-state and vibrationally excited states. The above theory provides a semiclassical approximation to the change in the band gap arising from nuclear motion [76].

In this work we use a quadratic approximation to $\hat{E}_g(\mathbf{q})$, which allows us to asses the importance of individual vibrational modes, to investigate microscopic mechanisms, and a Monte Carlo sampling method to calculate accurate numerical values of $E_g(T)$. In the quadratic approximation $\hat{E}_g(\mathbf{q})$ is approximated as

$$\hat{E}_g(\mathbf{q}) = \hat{E}_g(\mathbf{0}) + \sum_{n,\mathbf{k}} a_{n\mathbf{k}} q_{n\mathbf{k}}^2 \, . \tag{4}$$

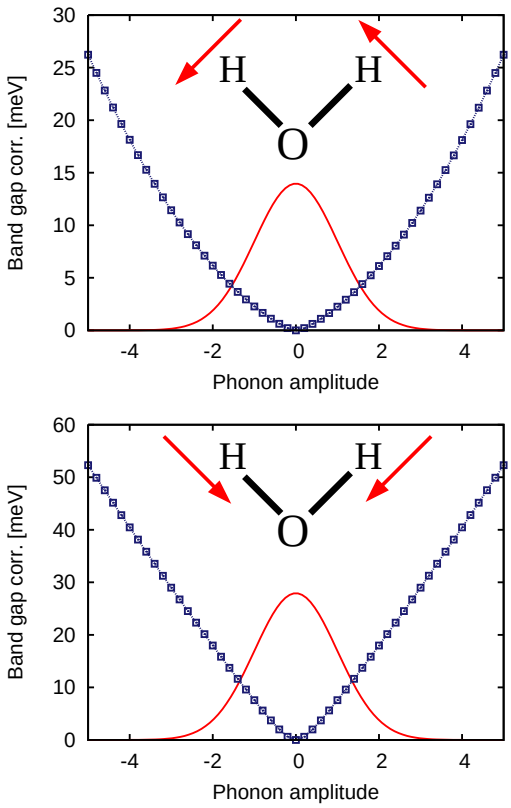

FIG. 2. Failure of the quadratic approximation for electron-phonon coupling for a librational (top) and a high frequency molecular symmetric O-H stretching mode (bottom). The strongly non-quadratic dependence of $\Delta\hat{E}_g(\mathbf{q})$ on the atomic positions $\mathbf{q}$ (blue) is particularly common for the librational and molecular modes of water ice. The harmonic vibrational density is shown in red.

The harmonic vibrational wave function is symmetric and odd terms in the polynomial expansion of $\hat{E}_g(\mathbf{q})$ vanish when evaluating the expectation value. Hence, the quadratic term is the first non-zero correction to the static band gap and errors are of $\mathcal{O}(\mathbf{q}^4)$. We calculate the diagonal quadratic coefficients, $a_{n\mathbf{k}}$, using a frozen phonon method, displacing the atoms by $\Delta q_{n\mathbf{k}}$ along phonon modes, and setting $a_{n\mathbf{k}} = (\hat{E}_g(\Delta q_{n\mathbf{k}}) + \hat{E}_g(-\Delta q_{n\mathbf{k}}))/(2\Delta q_{n\mathbf{k}}^2)$. We note that Eq. (4) is equivalent to the Allen-Heine-Cardona theory including off-diagonal Debye-Waller terms [77].

Although the quadratic approximation is valuable in obtaining atomistic insights, it does not produce accurate values of $E_g(T)$ for Ih and Ic. This arises because $\hat{E}_g(\mathbf{q})$ is generally not well described by a quadratic form, which also implies that the widely used Allen-Heine-Cardona theory is insufficient for studying electron-phonon coupling in ice. Examples of vibrational modes with particularly non-quadratic behaviour are shown in Fig. 2. Note that the non-quadratic dependence of the band gap on the atomic displacements is distinct from anharmonicity in nuclear vibrations and we therefore treat them inde-

pendently.

Instead of using the quadratic approximation to $\Delta\hat{E}_g(\mathbf{q})$, we therefore evaluate accurate values of $E_g(T)$ using Monte Carlo sampling, with N frozen phonon structures, $\{\mathbf{q}^i\}$, randomly drawn from the vibrational density, as $1/Z(T)\sum_{\mathbf{S}}|\phi_{\mathbf{S}}(\mathbf{q})|^2\exp(-\beta \mathrm{E}_{\mathbf{S}})$, which gives

$$E_g(T) = \frac{1}{N}\sum_{i=1}^{N}\hat{E}_g(\mathbf{q}^i). \tag{5}$$

N is typically larger than 500. The Monte Carlo approach includes all higher-order terms in $\hat{E}_g(\mathbf{q})$ neglected in the quadratic approximation and, unlike the quadratic approximation, remains valid for an anharmonic nuclear wavefunction.

In order to obtain finite temperature band-gap corrections we resample band-gap corrections using the finite temperature nuclear density with its wider tails.

To obtain the band gap correction due to anharmonic nuclear vibrations, on the other hand, we employ a reweighting approach as in Ref. [78], which is efficient and accurate for ice, since anharmonicity leads to a narrower, more localised nuclear density distribution. We reuse the band gap samples, $\hat{E}_g(\mathbf{q}^i_{\mathrm{har}})$, drawn from the harmonic vibrational density, $\left|\phi^{\mathrm{har}}(\mathbf{q})\right|^2/Z^{\mathrm{har}}(0)$, to calculate the band gap correction due to anharmonic nuclear vibrations as

$$E_g^{\mathrm{anh}}(T) = \frac{1}{N}\sum_{i=1}^{N} w_i \hat{E}_g(\mathbf{q}^i_{\mathrm{har}}), \tag{6}$$

where the weights, w_i, are calculated from the harmonic and anharmonic nuclear probability densities

$$w_i = \frac{\sum_{\mathbf{S}}\left|\phi^{\mathrm{anh}}_{\mathbf{S}}(\mathbf{q})\right|^2 \mathrm{e}^{-\beta \mathrm{E}^{\mathrm{anh}}_{\mathbf{S}}}/Z^{\mathrm{anh}}(T)}{\sum_{\mathbf{S}}\left|\phi^{\mathrm{har}}_{\mathbf{S}}(\mathbf{q})\right|^2 \mathrm{e}^{-\beta \mathrm{E}^{\mathrm{har}}_{\mathbf{S}}}/Z^{\mathrm{har}}(T)}. \tag{7}$$

As shown in Section V, including vibrational anharmonicity changes the vibrational band-gap correction, $\Delta E_g(T) = E_g(T) - \hat{E}_g(\mathbf{0})$, by only around 2 and 5 % in Ih and Ic, respectively, and (even up to the melting temperature) predominantly via the ZP band-gap correction. Hence, unless stated otherwise, all results were obtained using the harmonic approximation for the nuclear vibrations.

The same Monte Carlo approach could be employed to calculate vibrationally renormalised optical absorption spectra as demonstrated, for example, in Ref. [28]. For ice, excitonic effects would have to be included, for example, using the Bethe Salpeter equation [79], to obtain accurate optical absorption spectra. A first approximation at a much reduced computational cost could be obtained by simply adding the vibrational shift, $\Delta E_g(T)$, calculated in this work to the static lattice optical absorption spectra of Refs. [29] and [30]. Vibrationally renormalised optical absorption spectra of ice have not been calculated before, although they have been reported for other materials [80–82].

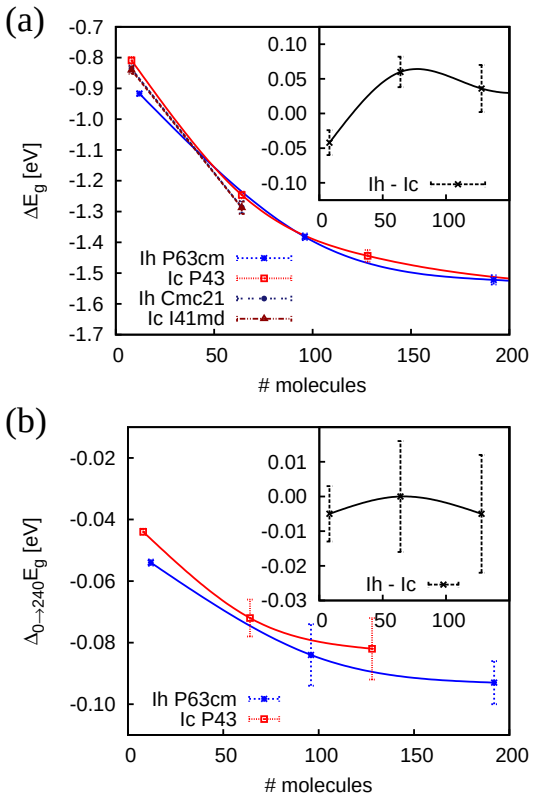

FIG. 3. Convergence of (a) the ZP band gap correction, $\Delta E_g(0)$, and (b) the thermal contribution $\Delta_{0\to T}E_g \equiv \Delta E_g(T) - \Delta E_g(0)$ with simulation cell size. The difference in $\Delta E_g(T)$ between Ih and Ic (and proton-orderings) converges rapidly with simulation cell size, even though the absolute $\Delta E_g(T)$ do not. This can be seen in the insets of (a) and (b), which show the difference in $\Delta E_g(0)$ and in $\Delta_{0\to 240}E_g(T)$ between Ih $P6_3cm$ and Ic $P4_3$, respectively. Comparing $\Delta E_g(0)$ of Ih $P6_3cm$, Ih $Cmc2_1$, Ic $P4_3$ and Ic $I4_1md$ shown in (a) provides further confirmation. The error bars indicate the statistical errors due to Monte Carlo sampling.

The absolute sizes of the vibrational corrections, $\Delta E_g(T)$, for different proton-orderings converge very slowly with the size of the simulation cell or, equivalently, with the density of the Brillouin Zone sampling (Figs. 3 (a) and (b), main panels). However, the differences in $\Delta E_g(T)$ between structures converge rapidly (Figs. 3 (a) and (b), insets). The relative $\Delta E_g(T)$ of various orthorhombic, 8-molecule proton-orderings are converged to better than around 50 meV. Despite the difference in shape and size of the simulation cell, the $\Delta E_g(T)$ of the hexagonal, 12-molecule Ih $P6_3cm$ proton-ordering is converged to within 75 meV relative to the orthorhombic, 8-molecule proton-orderings. This justifies the use of 8-molecule simulation cells in obtaining accurate relative band-gap corrections ΔE_g between different proton-orderings and between Ih and Ic. Supplementary Fig. S12 provides further support for this observation. We use simulation cells with up to 192 molecules to converge the absolute $\Delta E_g(T)$ with respect to simulation cell size

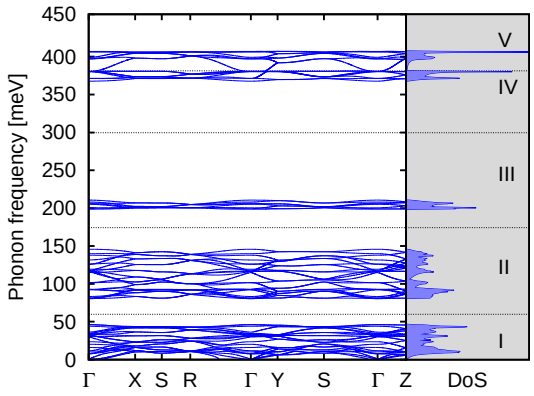

FIG. 4. Vibrational dispersion (left panel) and DoS (right panel) of 64-molecule Ih $Cmc2_1$. The DoS splits into crystal modes (I), librational modes (II), molecular bending modes (III) and molecular anti-symmetric (IV) and symmetric (V) O-H stretching modes. The soft modes along Γ →R are artifacts of k-point interpolation. Their contributions to the DoS is negligible and they do not affect the electron-phonon coupling results, which account only for vibrational modes commensurate with the Born-von Karman simulation cell. The vibrational dispersion and DoS of Ic are very similar to those of Ih.

to within 50 meV.

III. VIBRATIONAL BAND GAP RENORMALISATION

The vibrational density of states (DoS) of Ih (shown in Fig. 4) and Ic splits into five regimes: pseudo-translation modes (I), librational modes (II), molecular bending modes (III) and molecular (anti-) symmetric O-H stretching modes (IV and V). In Ref. [50] we showed that crystal modes (pseudo-translation and librational modes) and molecular modes (bending and O-H stretching modes) each contribute around half of the large band-gap correction in Ih $P6_3cm$ of around $\Delta E_g(0) \approx -1.5$ eV obtained for a 192-molecule simulation cell.

Figs. 5 (a) and (b) show $\Delta E_g(0)$ for protiated and deuterated 8-molecule proton-ordered Ih and Ic structures. The band-gap corrections are very similar in Ih and Ic. While the vibrational corrections, ΔE_g, shown in Fig. 5 (a) obtained for the 8-molecule unit cells are only converged to simulation cell size errors of around 0.75 eV, the relative ΔE_g of the proton-orderings are converged to less than 75 meV (see Section II and, in particular, Fig. 3), which is sufficient to distinguish between different proton-orderings.

Figs. 5 (a) and (b) show that nuclear vibrations largely average out differences in the band gaps obtained with different proton-orderings, reducing variations across proton-orderings in $E_g(0)$ by almost 3/4, i.e., from around 170 meV to $\leq$ 50 meV. This occurs because the protons are effectively smeared out by vibrational

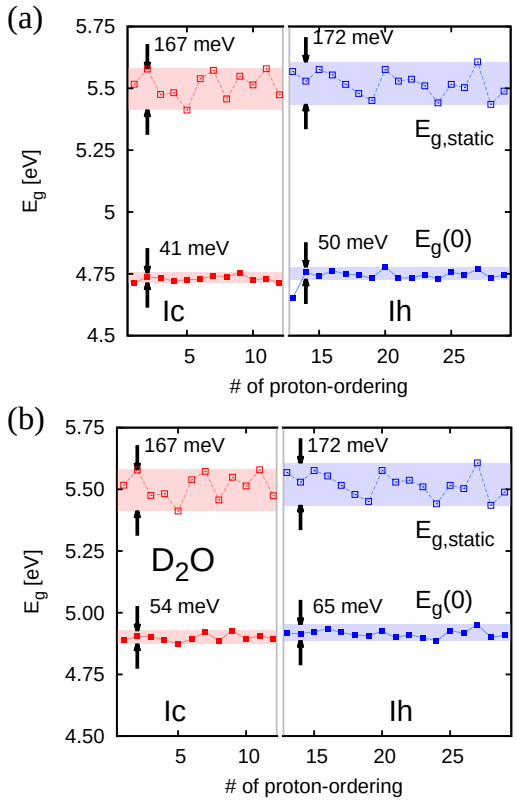

FIG. 5. Static-lattice band gaps, $E_{g,\mathrm{static}}$, and $E_g(0)$ of 8-molecule (a) H_2O and (b) D_2O proton-orderings. The change in the band gap due to vibrations (ΔE_g) of Ih and Ic are very similar. $\Delta E_g(0)$ for D_2O is significantly smaller than for H_2O. The ΔE_g for Ih $P6_3cm$ has been extrapolated down to a cell size of 8 molecules by fitting a 2nd order polynomial to the data points for 12, 96 and 192 molecules to compare it with the ΔE_g of the 8-molecule Ih and Ic proton-orderings.

motion. The root-mean-square (RMS) vibrational displacements of the protons of around 0.23Å correspond to about 1/3 of the difference in the bond length of an O-H covalent bond and an O$\cdots$H hydrogen bridge bond. While we did not remark on this in our earlier publication [27], this smearing effect also occurs in the free energies of proton-orderings, albeit in a far less striking way than for the band gaps. See Supplementary Section III [69] and Fig. S5 in particular for further details. The full static lattice and vibrationally renormalised bandstructures for 8-molecule Ih $Cmc2_1$ are shown in Fig. 6.

We find that the temperature dependence of $E_g(T)$ is almost independent of the proton-ordering. Fig. 7 (a) shows the temperature dependence of E_g for 8-molecule simulation cells of the Ih and Ic proton-orderings with the smallest and largest $\Delta E_g(0)$, respectively. In ice, even up to the melting temperature of 273 K, only the lowest frequency crystal vibrational modes (up to 24 meV) are thermally activated. These are long-wavelength modes that do not probe the differences between proton-orderings. As can be seen in Fig. 8, these low-energy crystal modes contribute less than one tenth of the ZP

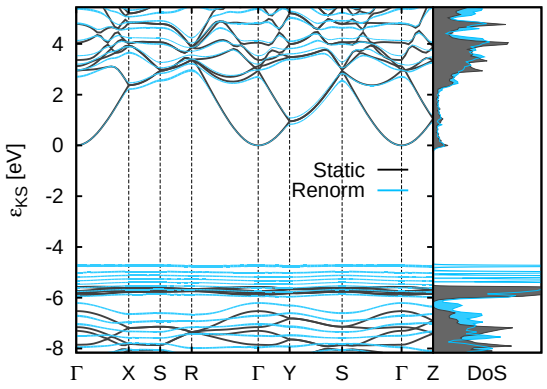

FIG. 6. Renormalisation of electronic bandstructure and DoS for 8-molecule Ih $Cmc2_1$. The conduction band minimum (CBM) has been set to zero energy. The broadening of the peak in the DoS at the top of the valence band indicates strong coupling of the phonons to the valence band maximum (VBM). Vice versa, the minimal broadening of the peaks at the bottom of the conduction band indicate weaker coupling of the phonons to the CBM. This picture remains if the energy of the lowest Kohn-Sham (KS) state is chosen as the reference instead of the CBM.

band-gap correction and accordingly the thermal correction up to melting at 273 K of around 95 meV is less than one tenth of the quantum ZP band-gap correction, $\Delta E_g(0)$. Notably, Ref. [35] reports the experimental observation of a shift in the (excitonic gap) of 85 ± 5 meV upon heating from 103 K to 254 K, which is in reasonable agreement with our calculated value of around 80 meV obtained for the 192-molecule Ih $P6_3cm$ simulation cell (see Fig. 7).

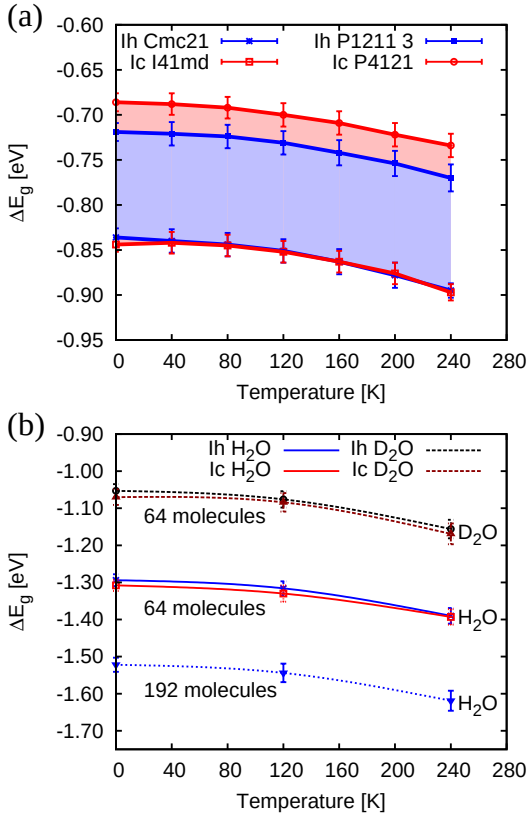

FIG. 7. (a) Temperature dependence of $E_g(T)$ for the protiated 8-molecule Ih and Ic proton-orderings with the largest and smallest values of $\Delta E_g(0)$, respectively. (b) Temperature dependence of $E_g(T)$ of 64-molecule H_2O and D_2O proton-orderings. $\Delta E_g(T)$ in Ih and Ic are very similar and the temperature dependence is just as strong in deuterated as in protiated ice. The most converged result for the 192-molecule Ih $P6_3cm$ structure is shown as a blue dotted line.

IV. DEUTERATED ICE

Deuteration of ice leads to a significant softening of all but the low frequency crystal vibrational modes. The resulting vibrational DoS is shown in panel (a) of Supplementary Fig. S8. The larger nuclear mass of deuterons in comparison to protons leads to smaller vibrational displacements. This isotope effect leads to a smaller ZP $\Delta E_g(0)$, as shown in Fig. 5 (b) for 64-molecule simulation cells. At the same time, the smaller deuteron vibrational displacements result in a smaller smearing out of the deuteron positions and thus a clearer distinction in $E_g(0)$ between different proton-orderings. The variations across proton-orderings increase from around 41–50 meV in protiated ice to 54–65 meV in deuterated ice. The thermal contribution to $\Delta E_g(T)$, $\Delta_{0\to T}E_g \equiv \Delta E_g(T) - \Delta E_g(0)$ in deuterated ice, however, is of comparable size to that in protiated ice (see Fig. 7 (b)). This follows from the very similar forms of the low frequency DoS of protiated and deuterated ice shown in panel (c) of Supplementary Fig. S8. The low frequency crystal modes up to frequencies of 24 meV, which become thermally activated at temperatures below 273 K, are collective modes for which the effect of the heavier deuterons is masked by the even heavier oxygen atoms. At high temperatures one might expect the higher ZP $\Delta E_g(0)$ in protiated ice to be reflected in a larger temperature dependence, but the crossover point at which all modes are thermally activated is far above melting.

V. THE ROLE OF VIBRATIONAL ANHARMONICITY

In Ref. [27] we showed that the effect of (typically quartic) anharmonicity in the Born-Oppenheimer energy surface is to localise the nuclear wavefunctions by 1.5% and 2.5% with respect to the harmonic wavefunctions of Ih and Ic, respectively. This can be understood as a reduction of the anharmonic vibrational displacements, $q^{\rm anh}_{n\mathbf{k}}$, with respect to the harmonic vibrational displacements, $q^{\rm har}_{n\mathbf{k}}$, by a factor $\alpha = 0.985$ and $\alpha = 0.975$ for Ih and Ic, respectively: $q^{\rm anh}_{n\mathbf{k}} = \alpha q^{\rm har}_{n\mathbf{k}}$. Since the de-

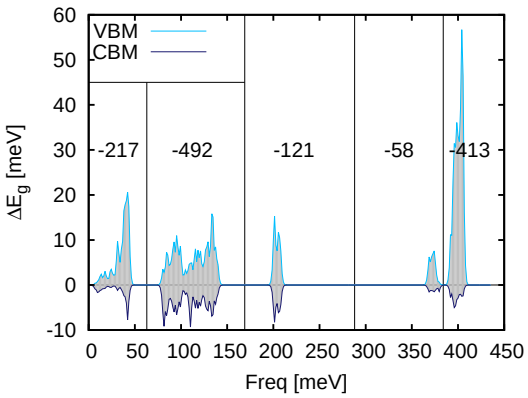

FIG. 8. Contributions of vibrational modes to $\Delta E_g(0)$ for 64-molecule Ih $Cmc2_1$. Unlike the band gap and, consequently, the vibrational corrections to it, the individual vibrational corrections to the KS energies of the VBM and CBM cannot be measured, but can be understood in terms of the VBM and CBM electronic densities shown in Fig. 9.

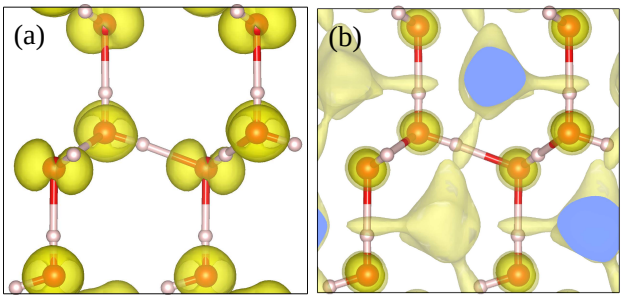

FIG. 9. (a) VBM and (b) CBM electronic densities of Ih $Cmc2_1$. The electronic charge density of the VBM is localised in oxygen lone-pair-like orbitals which form the hydrogen bridge network. Thus the VBM couples strongly to the molecular and librational modes. The CBM is delocalised (pale yellow isosurface), but the bulk of the electron density is localised in orbitals of anti-bonding $\sigma^\star$ character, centered on the oxygen nuclei.

pendence of the band gap on $q_{n,\mathbf{k}}$ is typically well approximated by $\Delta\hat{E}_g(q_{n\mathbf{k}}) \approx c^{(1)}_{n\mathbf{k}}|q_{n\mathbf{k}}| + c^{(2)}_{n\mathbf{k}}|q_{n\mathbf{k}}|^2$ (see Fig. 2) we expect the anharmonic band-gap correction in Ih, $\Delta\hat{E}^{\mathrm{anh}}_g(q_{n\mathbf{k}}) \approx \alpha\left(c^{(1)}_{n\mathbf{k}}|q^{\mathrm{har}}_{n\mathbf{k}}| + \alpha c^{(2)}_{n\mathbf{k}}|q^{\mathrm{har}}_{n\mathbf{k}}|^2\right)$, to be between α of the harmonic value, $\Delta E^{\mathrm{har}}_g$, if $c^{(1)}_{n\mathbf{k}} \gg c^{(2)}_{n\mathbf{k}}$ to α^2 of the harmonic value if $c^{(2)}_{n\mathbf{k}} \gg c^{(1)}_{n\mathbf{k}}$. Correspondingly, we expect anharmonic corrections to the band gap of +1.5% to +2.25% of the $\Delta E^{\mathrm{har}}_g$. Similarly we expect corrections in Ic of +2.5% to +6.25% of the harmonic ΔE_g. The harmonic band-gap correction is around −1.5 eV for Ih and Ic, which translates into expected zero-temperature band-gap corrections due to anharmonicity of around 20–35 meV and 40–90 meV for Ih and Ic, respectively. Using the reweighting procedure described in Section II D, we calculate anharmonic corrections to $E_g(0)$ of $+33 \pm 18$ meV and $+76 \pm 21$ meV for Ih and Ic, respectively, in good agreement with the estimates given above. We use the 96-molecule Ih $P6_3cm$ and the 64-molecule Ic $P4_3$ simulation cells.

We note that the band gap corrections due to vibrational anharmonicity in Ih and Ic, and different proton-orderings, only differ by around 20 meV. Hence the variations in E_g across proton-orderings remain small at around 50 meV, independent of whether anharmonic nuclear motion is included.

VI. ATOMISTIC INSIGHTS

As shown in Fig. 8, the pseudo-translations (0–50 meV), molecular bending modes (195–214 meV) and anti-symmetric O-H bond stretching modes (363–384 meV) together contribute less than 1/3 of $\Delta E_g(0)$ (the individual contributions are around 16%, 10% and 4%, respectively). Librational modes (76–150 meV) and symmetric O-H bond stretching modes (387–411 meV) give large contributions of around 38% and 32%, respectively.

Overall, the vibrational motion of the nuclei predominantly couples to the valence band maximum (VBM), as shown in Fig. 6, in which the peaks corresponding to the valence band states are strongly renormalised and broadened, while the peaks corresponding to the conduction band states remain relatively sharp and distinct. The electron density corresponding to the VBM sits in distorted oxygen lone pair orbitals (see Fig. 9 (a)). Consequently, the electronic density corresponding to the VBM is significantly distorted by displacements of the protons along their O-H covalent and O···H bridge bonds. Such displacements arise, in particular, from the symmetric O-H bond stretching modes, which therefore strongly affect the Kohn-Sham (KS) energy of the VBM.

Librational modes also couple to the VBM, albeit less strongly. Unlike the O–H bond stretching modes, librational modes additionally couple significantly to the conduction band minimum (CBM). The electron density corresponding to the CBM is predominantly localised in orbitals of anti-bonding $\sigma^\star$ character centered on the oxygen nuclei (see Fig. 9 (b)). These are almost identical for different proton-orderings, due to their practically identical oxygen sublattices (up to a difference in stacking of layers between Ih and Ic). Consequently the electron density corresponding to the CBM is very similar for all proton-orderings. Unlike the O-H bond stretching modes, the librational modes distort the oxygen sublattice with respect to the static configuration, momentarily (though not on average) breaking the tetrahedral coordination of the oxygen atoms and affecting the electron density forming the CBM. Nonetheless, the coupling of the vibrational motion of the nuclei to the CBM is weak due to the atomic-like nature of the electron density of the CBM.

Besides leading to the largest contribution to $\Delta E_g(0)$, O–H stretching modes also play the predominant role in

smearing out the distinction between proton-orderings, thereby making the VBM energies of different proton-orderings more similar. This effect of reducing differences in $\Delta E_g(0)$ between proton-orderings is clearly shown in Fig. 5. While the strong renormalisation of the KS energy of the VBM leads to strong vibrational renormalisation of E_g, the free energy (which corresponds to the sum over all vibrationally renormalised occupied KS bands) is much less affected. Consequently the narrowing of the distribution of lattice free energies of different proton-orderings is far less pronounced than for the band gaps (see Supplementary Section III).

VII. CONCLUSIONS

Accurate static lattice electronic band gaps can be calculated using theoretical methods such as DFT with semi-local or hybrid functionals, the *GW* method, or highly accurate quantum chemical methods. However, it is important to account for vibrational effects when benchmarking calculated electronic band gaps against experiment. We have found vibrational corrections to the static electronic band gaps of water ice of -1.5 to -1.7 eV, which are significant on the scale of the differences between results obtained with these methods and compared to the size of the experimental gap.

Proton-disorder, on the other hand, does not play an important role in determining the electronic bandstructure of Ih and Ic. The use of different proton-orderings in an atomistic simulation affects the energetics of Ih and Ic on the scale of the difference in free energy between Ih and Ic. However, when vibrations are accounted for, the renormalised zero and finite temperature electronic bandstructures of different proton-ordered Ih and Ic structures are very similar. Hence, atomistic simulations of band gaps and optical absorption spectra depend only weakly on the proton-ordering when vibrations are taken into account. The similarity of the vibrationally renormalised electronic bandstructures of different Ih and Ic proton-orderings also implies that measurements of the band gaps or optical absorption spectra of ice samples are not capable of distinguishing between proton-orderings or between Ih, Isd and Ic. Comparing experimental band gaps of protiated and deuterated ice would provide a straightforward means of accessing quantum zero-point effects. Such measurements might allow the resolution of the predicted difference in the band gaps of protiated and deuterated ice of around 0.2 eV.

Non-quadratic behaviour plays a crucial role in water ice. For example, accurate vibrationally renormalised electronic band gaps can only be calculated by carefully accounting for the strongly non-quadratic dependence of the band gap on the vibrational displacements. In fact, if accuracies of tens of meV for electronic band gaps are to be achieved, vibrational anharmonicity must be accounted for as well. Anharmonic nuclear vibrations are crucial in understanding the relative stability of Ih and Ic [27] and many other phenomena. It would be of great interest to study the role of anharmonicity at ice surfaces and in the presence of impurities or other defects.

Acknowledgements. We acknowledge financial support from the Engineering and Physical Sciences Research Council of the UK [EP/J017639/1]. B. M. also acknowledges Robinson College, Cambridge, and the Cambridge Philosophical Society for a Henslow Research Fellowship. The calculations were performed using the Cambridge High Performance Computing Service facility and the Archer facility of the UK's national high-performance computing service (for which access was obtained via the UKCP consortium [EP/K013564/1]).

[1] H. Weingärtner and E. Franck, Angew. Chem. Int. Ed., **44**, 2672 (2005).
[2] A. Liebscher, Geofluids, **10**, 3 (2010).
[3] T. Bartels-Rausch, V. Bergeron, J. H. E. Cartwright, R. Escribano, J. L. Finney, H. Grothe, P. J. Gutiérrez, J. Haapala, W. F. Kuhs, J. B. C. Pettersson, S. D. Price, C. I. Sainz-Díaz, D. J. Stokes, G. Strazzulla, E. S. Thomson, H. Trinks, and N. Uras-Aytemiz, Rev. Mod. Phys., **84**, 885 (2012).
[4] M. B. Baker and T. Peter, Nature, **451**, 299 (2008).
[5] K. C. Young, *Microphysical Processes in Clouds.* (Oxford University Press, New York, 1993).
[6] C. George *et al.*, *Atmospheric and Aerosol Chemistry*, edited by V. F. McNeill and P. A. Ariya (Springer, 2014).
[7] E. A. Betterton and D. J. Anderson, J. Atmos. Chem., **40**, 171 (2001).
[8] A. M. Grannas *et al.*, Atmos. Chem. Phys., **7**, 4329 (2007).
[9] D. Heger, J. Jirkovsky, and P. Klan, J. Phys. Chem. A, **109**, 6702 (2005).
[10] N. Takenaka and H. Bandow, J. Phys. Chem. A, **111**, 8780 (2007).
[11] N. Takenaka, A. Ueda, and Y. Maeda, Nature, **358**, 736 (1992).
[12] S.-C. Park, E.-S. Moon, and H. Kang, Phys. Chem. Chem. Phys., **12**, 12000 (2010).
[13] C. S. Boxe, A. J. Colussi, M. R. Hoffmann, I. M. Perez, J. G. Murphy, and R. C. Cohen, J. Phys. Chem. A, **110**, 3578 (2006).
[14] T. F. Kahan and D. J. Donaldson, J. Phys. Chem. A, **111**, 1277 (2007).
[15] J. Klanova, P. Klan, J. Nosek, and I. Holoubek, Environ. Sci. Technol., **37**, 1568 (2003).
[16] M. P. Bishop *et al.*, *Encyclopedia of Snow, Ice and Glaciers*, edited by V. P. Singh, P. Singh, and U. K. Haritashya (Springer, 2011).
[17] D. Chandler, *Classical and Quantum Dynamics in Condensed Phase Simulations.*, edited by B. J. Berne, G. Ci-

ccotti, and D. F. Coke (World Scientific, 1998).
[18] R. A. Marcus, J. Chem. Phys., **24**, 966 (1956).
[19] C. S. Cucinotta, I. Rungger, and S. Sanvito, J. Phys. Chem. C, **116**, 22129 (2012).
[20] J. Hama, Y. Shiomi, and K. Suito, J. Phys. Condens. Matter, **2**, 8107 (1990).
[21] C. Cavazzoni *et al.*, Science, **283**, 4446 (1999).
[22] T. R. Mattsson and M. P. Desjarlais, Phys. Rev. Lett., **97**, 017801 (2006).
[23] A. Hermann, N. Ashcroft, and R. Hoffmann, Proc. Natl Acad. Sci., **109**, 745750 (2012).
[24] C. J. Pickard, M. Martinez-Canales, and R. J. Needs, Phys. Rev. Lett., **110**, 245701 (2013).
[25] D. Pan, Q. Wan, and G. Galli, Nature Commun., **5**, 3919 (2014).
[26] N. F. Ness *et al.*, Science, **233**, 85 (1986).
[27] E. A. Engel, B. Monserrat, and R. J. Needs, Phys. Rev. X, **5**, 021033 (2015).
[28] M. Zacharias, C. E. Patrick, and F. Giustino, Phys. Rev. Lett., **115**, 177401 (2015).
[29] P. H. Hahn, W. G. Schmidt, K. Seino, M. Preuss, F. Bechstedt, and J. Bernholc, Phys. Rev. Lett., **94**, 037404 (2005).
[30] C. Fang, W.-F. Li, R. S. Koster, J. Klimeš, A. van Blaaderen, and M. A. van Huis, Phys. Chem. Chem. Phys., **17**, 365 (2015).
[31] S. G. Warren, Applied Optics, **23**, 1206 (1984).
[32] A. P. Minton, J. Phys. Chem., **75**, 1162 (1971).
[33] L. R. Painter, R. D. Birkhoff, and E. T. Arakawa, J. Chem. Phys., **51**, 243 (1969).
[34] M. Seki, K. Kobayashi, and J. Nakahara, J. Phys. Soc. Jap., **50**, 2643 (1981).
[35] T. Shibaguchi, H. Onuki, and R. Onaka, J. Phys. Soc. Jap., **42**, 152 (1977).
[36] J. Paier, M. Marsman, K. Hummer, G. Kresse, I. C. Gerber, and J. G. Ángyán, J. Chem. Phys., **124**, 154709 (2006).
[37] S. J. Clark and J. Robertson, Phys. Rev. B, **82**, 085208 (2010).
[38] L. Hedin, Phys. Rev., **139**, 796 (1965).
[39] L. Hedin and S. Lundqvist, *Solid State Physics.*, edited by F. Seitz, D. Turnbull, and H. Ehrenreich (Academic Press, 1969).
[40] M. S. Hybertsen and S. G. Louie, Phys. Rev. Lett., **55**, 1418 (1985).
[41] R. W. Godby, M. Schlüter, and L. J. Sham, Phys. Rev. B, **37**, 10159 (1988).
[42] W. G. Aulbur, L. Jonsson, and J. W. Wilkins, Solid State Physics, **54**, 1 (2000).
[43] C. J. Cramer, *Essentials of Computational Chemistry* (Wiley & Sons, Inc., 2002) pp. 191–232.
[44] I. Shavitt and R. J. Bartlett, *Many-Body Methods in Chemistry and Physics: MBPT and Coupled-Cluster Theory* (Cambridge University Press, 2009).
[45] D. M. Ceperley and B. J. Alder, Phys. Rev. Lett., **45**, 566 (1980).
[46] W. M. C. Foulkes, L. Mitas, R. J. Needs, and G. Rajagopal, Rev. Mod. Phys., **73**, 33 (2001).
[47] R. J. Needs, M. D. Towler, N. D. Drummond, and P. López Ríos, J. Phys.: Cond. Mat., **22**, 023201 (2010).
[48] N. D. Drummond, A. J. Williamson, R. J. Needs, and G. Galli, Phys. Rev. Lett., **95**, 096801 (2005).
[49] A. J. Williamson, R. Q. Hood, R. J. Needs, and G. Rajagopal, Phys. Rev. B, **57**, 12140 (1998).
[50] B. Monserrat, E. A. Engel, and R. J. Needs, Phys. Rev. B: Rapid Commun., **92**, 140302(R) (2015).
[51] C. Sanchez-Valle, D. Mantegazzi, J. Bass, and E. Reusser, J. Chem. Phys., **138**, 054505 (2013).
[52] B. Monserrat, G. J. Conduit, and R. J. Needs, Phys. Rev. B, **90**, 184302 (2014).
[53] J. D. Bernal and R. H. Fowler, J. Chem. Phys., **1**, 515 (1933).
[54] H. König, Z. Kristallogr., **105**, 279 (1944).
[55] B. J. Murray, D. A. Knopf, and A. K. Bertram, Nature, **434**, 202 (2005).
[56] J. E. Shilling, M. A. Tolbert, O. B. Toon, E. J. Jensen, B. J. Murray, and A. K. Bertram, Geophys. Res. Lett., **33**, L17801 (2006).
[57] T. L. Malkin, B. J. Murray, C. G. Salzmann, V. Molinero, S. J. Pickering, and T. F. Whale, Phys. Chem. Chem. Phys., **17**, 60 (2015).
[58] W. F. Kuhs, C. Sippel, A. Falenty, and T. C. Hansen, Proc. Nat. Acad. Sci. U.S.A., **109**, 21259 (2012).
[59] T. H. G. Carr, J. J. Shephard, and C. G. Salzmann, J. Phys. Chem. Lett., **5**, 2469 (2014).
[60] L. Pauling, J. Am. Chem. Soc., **57**, 2680 (1935).
[61] Y. Tajima, T. Matsuo, and H. Suga, Nature, **299**, 810 (1982).
[62] S. M. Jackson and R. W. Whitworth, J. Phys. Chem. B, **101**, 6177 (1997).
[63] J. F. Nagle, J. Math. Phys., **7**, 1484 (1966).
[64] C. P. Herrero and R. Ramírez, J. Chem. Phys., **140**, 234502 (2014).
[65] K. Hirsch and L. Ojamäe, J. Phys. Chem. B, **108**, 15856 (2004).
[66] Z. Raza, D. Alfè, C. G. Salzmann, J. Klimeš, A. Michaelides, and B. Slater, Phys. Chem. Chem. Phys., **13**, 19788 (2011).
[67] J. Lekner, Physica B: Cond. Mat., **252**, 149 (1998).
[68] S. J. Singer, J. Kuo, T. K. Hirsch, C. Knight, L. Ojamäe, and M. L. Klein, Phys. Rev. Lett., **94**, 135701 (2005).
[69] See Supplemental Material at http://... for more information on the convergence of the band gap corrections with the simulation cell size, the failure of the quadratic approximation for the electronic band gap in ice, vibrational averaging over proton-orderings, the atomistic picture, the choice of the exchange-correlation functional and the effects of unit cell expansion, correlated sampling for the temperature dependence of the band gap, and the effects of large vibrational displacements on band gap measurements.
[70] S. J. Clark, M. D. Segall, C. J. Pickard, P. J. Hasnip, M. I. J. Probert, K. Refson, and M. C. Payne, Z. Kristallogr., **220**, 567 (2005).
[71] J. P. Perdew, K. Burke, and M. Ernzerhof, Phys. Rev. Lett., **77**, 3865 (1996).
[72] B. Santra, J. Klimeš, A. Tkatchenko, D. Alfè, B. Slater, A. Michaelides, R. Car, and M. Scheffler, J. Chem. Phys., **139**, 154702 (2013).
[73] D. Vanderbilt, Phys. Rev. B, **41**, 7892 (1990).
[74] K. Kunc and R. M. Martin, Phys. Rev. Lett., **48**, 406 (1982).
[75] B. Monserrat, N. D. Drummond, and R. J. Needs, Phys. Rev. B, **87**, 144302 (2013).
[76] C. E. Patrick and F. Giustino, J. Phys.: Cond. Mat., **26**, 365503 (2014).
[77] X. Gonze, P. Boulanger, and M. Côté, Ann. Phys., **523**,

168 (2011).
[78] B. Monserrat, R. J. Needs, and C. J. Pickard, J. Chem. Phys., **141**, 134113 (2014).
[79] H. Bethe and E. Salpeter, Phys. Rev., **84**, 1232 (1951).
[80] A. Marini, Phys. Rev. Lett., **101**, 106405 (2008).
[81] J. Noffsinger, E. Kioupakis, C. G. Van de Walle, S. G. Louie, and M. L. Cohen, Phys. Rev. Lett., **108**, 167402 (2012).
[82] C. E. Patrick and F. Giustino, J. Phys.: Cond. Matt., **26**, 365503 (2014).
[83] M. Schönherr and B. Slater and J. Hutter and J. VandeVondele, J. Phys. Chem. B, **118**, 590 (2014).